Virtual image correlation of magnetic resonance images for 3D geometric modelling of pelvic organs

Zhifan Jiang, Olivier Mayeur, Jean-Francois Witz, Pauline Lecomte-grosbras, Jérémie Dequidt, Michel Cosson, Christian Duriez, Mathias Brieu

Received <day> <month>, <year>; | Revised <day> <month>, <year>; | Accepted <day> <month>, <year>

DOI: xxx/xxxx

FULL PAPER

Virtual Image Correlation of Magnetic Resonance Images for 3D Geometric modelling of Pelvic Organs

Z. Jiang[1,2,3] | O. Mayeur[1,2] | J.-F. Witz[1,2] | P. Lecomte-Grosbras[1,2] | J. Dequidt[3] | M. Cosson[1,4,5] | C. Duriez[6] | M. Brieu[1,2]

[1]Laboratoire de Mécanique de Lille, CNRS FRE-3723, France
[2]Centrale Lille, France
[3]Univ. Lille, UMR 9189 - CRIStAL - Centre de Recherche en Informatique Signal et Automatique de Lille, France
[4]CHU Lille, Service de Chirurgie Gynécologique, France
[5]Univ. Lille, Faculté de Médecine,France
[6]Inria Lille-Nord-Europe, France

Correspondence
*Z. Jiang, Email: zhifan.jiang@gmail.com

Numerical simulation of pelvic system could lead to a better understanding of common pathology, through objective and reliable analyses of pelvic mobility, according to mechanical principles. In clinical context, patient-specific simulation has the potential for a proper patient-personalized cure. For this purpose, a simulable 3D geometrical model, well suited to patient anatomy, is required. However, the geometric modelling of pelvic system from medical images (MRI) is a complex operator-dependent and time-consuming process, not adapted to patient-specific applications. This paper is addressing this challenging computational problem. The objective is to develop a technique providing a smooth, consistent and readily usable 3D geometrical model, seamlessly from image to simulation. In this paper, we use a generic topologically-simplified B-Spline model to represent pelvic organs. The presented paper develops a Virtual Image Correlation (VIC) method to find the best correlation between the geometry and the image. The final reconstructed geometrical model is to be compatible with meshing and Finite Element (FE) simulation. Then, a variety of tests are performed to prove the concept, through both prototypical and pelvic models. Finally, since the pelvic system is complex, including structures hardly identifiable in MRI, some feasible solutions to introduce more complex pelvic models are also discussed.

KEYWORDS:
3D geometry, B-Spline, geometric modelling, MRI, pelvic system, virtual image correlation

1 | INTRODUCTION

Common pelvic floor dysfunctions, such as genital prolapse or endometriosis, correlate strongly with pelvic mobility [4, 7]. In order to better understand the mechanism of pathology through the mobility, the numerical simulation of the pelvic system has received much attention in recent years. Such simulations allow to perform objective and quantitative analyses, subject to mechanical principles [17, 22]. In addition to the pelvic system, these numerical techniques have received also much attention for other structures of the human body, such as blood flow [35] and the femur [26].

In the clinical context, patient-specific simulations would help to provide better personalized treatment to patients. The simulation requires firstly 3D geometrical models corresponding to patient anatomy. The 3D geometric modelling from medical image data is generally problematic, which becomes a major challenge in computational biomechanics for medicine. In [35], a parametric modelling was proposed for isogeometric analysis [6] of the blood flow. In this paper, we are dealing with the issue of geometric modelling, taking into account the particularities of the pelvic system.

Our objective of geometric modelling consists in creating consistent and readily usable 3D geometries for Finite Element (FE) simulations. Because of its high contrast for soft tissue analysis, Magnetic Resonance Imaging (MRI) has become the principal choice for the examination of pelvic pathologies [8]. Being consistent with the medical reality, our MRI acquisition protocols are similar to the ones used in clinical trials, which include multi-slices 2D static MRI for spatial anatomy information and also a sequence of 2D dynamic MRI for temporal information (motion). Usually, the medium image resolution and anisotropic voxels are not ideal for processing. The geometric modelling of pelvic organs from static MRIs is highly influenced by the quality of images. The reconstructed geometry should firstly represent the shape of the organs in images. Moreover, some suspension devices (fasciae and ligaments) are difficult to be observed in MRI. In addition to matching the geometry of multiple organs (bladder, vagina and rectum), a viable geometrical model must be adapted to satisfy multiple criteria for FE simulations: smoothness with support of NURBS (NonUniform Rational B-Spline) surfaces [24] for meshing, identifiable boundaries on subsets of geometry for defining loadings and contacts between organs, fasciae and ligaments etc.

So far, such reconstruction procedure subjects an experienced operator to days of modelling. The procedure includes two main operator-dependent steps: (i) manual segmentation on MRI to obtain 3D representation of the pelvic system (labelled voxels); (ii) manual correction and creation of surface model using a CAD (Computer-Aided Design) software [21].

Concerning the step (i), a variety of algorithms have been proposed to extract from original images segmented volumes, represented by labelled voxels. These techniques vary from thresholding [18] to more sophisticated mathematical models (a non-exhaustive survey can be found in [23]). However, such voxel-based techniques cannot directly create surface models. Generally, an iso-surface generation algorithm, like Marching Cubes or its advanced version [19, 33], is applied to build 3D surfaces, represented by point cloud or raw mesh. This procedure has become a standard implemented tool in a lot of image processing software, such as AVIZO (https://www.fei.com/software/amira-avizo/) and 3DSlicer [13]. However, the terracing artefact on these triangular meshes has been a common issue, especially when the image data contain highly anisotropic voxels as in our case. Thus, the generated surface models cannot be used directly in FE simulations. For this reason, the step (ii) is necessary to create simulable geometrical models. This time-consuming and highly human-dependent process is, nevertheless, not suitable for patient-specific applications in the clinical routine. Moreover, the smoothing and repairing involved in step (ii) are performed separately, which are no longer linked with image data.

To deal with the issue, another approach has been considered to merge the two steps: Model-to-Image Registration. Such deformable model-based approach was firstly introduced in [12]. A geometric contour defined by points was optimized to find the best correlation with image. This technique was then improved and developed on different aspects: from geometry representation to cost functions (image energy) [34, 20]. A class of more successful techniques consists in defining the deformable geometry in an appropriate shape space, named Statistical Shape Models (SSM), firstly introduced in [5]. These techniques have proved interesting in a multitude of applications [9]. Particular attention should be paid to the representation of shapes and their comparison with images [16]. Building such a complex model as the pelvic system, which has multiple structures and high inter-variability, would thus require a large training set and a significant number of extra works.

Alternatively, a registration method called Virtual Image Correlation (VIC) has been proposed to detect objects in 2D images captured during mechanical experiments, using a deformable parametric geometry [31, 25]. The virtual image is generated as an intensity profile linked with the geometry and is compared to the real image intensity. The correlated geometry is smooth and circumvents the deficiency related to image resolution or noises. A virtual image can be computed with any parametric geometry, such as B-Spline, which is suitable in our case. In addition, the problem can be written as a minimization formulation, the same as a classical image registration problem. By replacing the geometry representation, the method would allow us to perform a Model-to-Image Registration with the pelvic model to achieve our objectives.

In [11, 10], we adapted the VIC technique to create the flexible 2D geometrical model of pelvic organs on 2D static MRIs, and to track these organs on the temporal sequence of 2D dynamic MRIs. In this paper, we are presenting this technique in the case of the 3D parametric reconstruction of geometrical models. Consistent with our objectives, the major contribution is to perform 3D geometric modelling from MRI to provide efficiently and directly 3D FE models (for meshing and simulation), without extra smoothing and surface creation. However, at this stage, we use a topologically-simplified B-Spline model to demonstrate our method. In the remainder of this paper, we will present the methodology of 3D VIC: parametrization of geometry, generation of virtual image and optimization. A special contribution will then be performed to prove the method, through a batch of tests with both prototypical and real pelvic models. In the Discussion part, we will also provide feasible solutions to compute more complex 3D pelvic geometries, including structures other than organs, as aforementioned.

2 | 3D VIRTUAL IMAGE CORRELATION

The methodology of 3D VIC contains five main components:

- input image data (MRI)
- generic geometrical model (B-Spline surfaces to be deformed)
- virtual image (associated to the geometry)
- cost function (comparison between virtual image and real one)
- optimization (finding the best correlation between two images)

Firstly, based on the definition of geometry, its parametrization should be decided. These are degrees of freedom (DOF) to be changed while the geometry is being deformed. Secondly, a virtual image is computed in the neighbourhood of the B-Spline surface. The variation of intensity of the virtual image is defined by a continuous level set function, which simulates a gradual change in gray level from inside to outside of the surfaces. Then, a cost function is used to compare the two images, such as the squared difference of gray levels. Finally, an optimization algorithm is applied to minimize iteratively the cost function, so that the controlled geometry fits the real image. The relation between the geometry, DOF and virtual image can be built analytically, which will be presented later.

Figure 1 illustrates a female pelvic system with an MRI acquisition according to this area. Intravaginal and intrarectal gel had been introduced to highlight the vagina and rectum. Meanwhile, the bladder was replete with water (Figure 1 (b,c)). The presented MRI was performed on a healthy witness, with a spatial resolution of 0.59 mm pixel^{-1} and the thickness of the slice is 4 mm. MRI acquisitions on other patients follow a similar protocol. Multi-slice 2D MRIs in three directions (sagittal, transverse and coronal) are in our possession. Usually, the coronal planes are less representative and more confusing, and are thus not used to apply segmentation. Besides, the uterus is not involved in our numerical simulation. Whereas, as mentioned in Section 1, the blue parts in Figure 1 (a) (suspension structures) are modelled for FE simulation, but they are difficult to be identified in MRI. In the next sections, we will explain the other four main parts of registration respectively.

2.1 | Geometry definition and parametrization

Generally, for a 3D FE model, the geometry is defined by NURBS surfaces [24], which is the case of most CAD modellings for numerical simulation. The complete 3D CAD model of pelvic system is quite complex, a topologically-simplified geometry is thus used to demonstrate our method . Each geometry is defined using a single-patch B-Spline surface. Such model circumvents the difficulty to ensure continuity along the edges of multiple patches, and contains a limited number of control points. Meanwhile, it remains totally consistent with our Model-to-Image Registration framework.

Given a bidirectional control net $\{\mathbf{p}_{i,j}|(i,j) \in \{0,\cdots,n\} \times \{0,\cdots,m\}\}$, where $\mathbf{p}_{i,j}$ denotes a control point, a B-Spline patch is obtained by computing a tensor product surface. Hence, a surface point at parameter values (u,v) is given by the following formulation:

$$\mathcal{S}(u,v) = \sum_{i=0}^{n}\sum_{j=0}^{m} \mathcal{N}_{i,p}(u)\mathcal{N}_{j,q}(v)\mathbf{p}_{i,j}, \forall (u,v) \in [0,1]^2 \quad (1)$$

where $\mathcal{N}_{i,p}$ and $\mathcal{N}_{j,q}$ are B-Spline basis functions of degree p and q, respectively. Each organ is modelled by a closed 2D surface embedded in 3D. Figure 2 illustrates how a $(n+1)\times(m+1)$ control net is closed to form a single-patch surface. Additional constraints should also be applied to ensure continuity at connections. For example, the following conditions imply the $\mathcal{C}^1$ continuity on the side (E_3 and E_4 in Figure 2):

$$\overrightarrow{\mathbf{p}_{n,j}\mathbf{p}_{0,j}} = \overrightarrow{\mathbf{p}_{0,j}\mathbf{p}_{1,j}} \quad \forall j \in [0,m].$$

Figure 3 shows a 3D visual example of the organ's geometry, control points are joined together to form the top and lateral connection. $\mathbf{p}_{0,6}$ and $\mathbf{p}_{0,0}$ are repeated 9 times, they must remain joined during optimization. The control points $\{\mathbf{p}_{0,j}\}$ corresponding to other j values have the same constraint to keep the lateral connection closed. In addition, their neighbouring points $\{\mathbf{p}_{i,5}\}$ and $\{\mathbf{p}_{i,1}\}$ should be coplanar to ensure the smoothness at the top and bottom. For other j value $\bar{j}$, $\mathbf{p}_{0,\bar{j}}$, $\mathbf{p}_{1,\bar{j}}$ and $\mathbf{p}_{7,\bar{j}}$ should remain collinear for the same reason. The surface normals can be evaluated by using the tangents in $u-$ and $v-$ direction. However, it becomes problematic at the poles. Geometrically at the poles, the normal will be perpendicular to the common plane. However, these normals (because of the singularity) are not used for computing the virtual image. The virtual image and cost function are evaluated in a subset of sampled points.

The geometry definition and parametrization are two different concepts. The first was presented in the previous paragraph, which allows to find geometrical properties, based on a mathematical model, either discrete, implicit, or parametric. The second concept consists in using DOFs (or parameters) to determine the shape of a particular surface, usually in a reduced dimension space. Hence, the variability of forms is limited by the space dimension and the value of DOFs will be computed via an optimization procedure.

Mathematically, a surface embedded in 3D is a set of points $\mathcal{S} \subset \mathbb{R}^3$, the parametrization of which is such a function $\mathcal{P} : A \rightarrow \{\mathcal{S}\}$, where A is the parameter space. In this paper, we use two principal parametrizations:

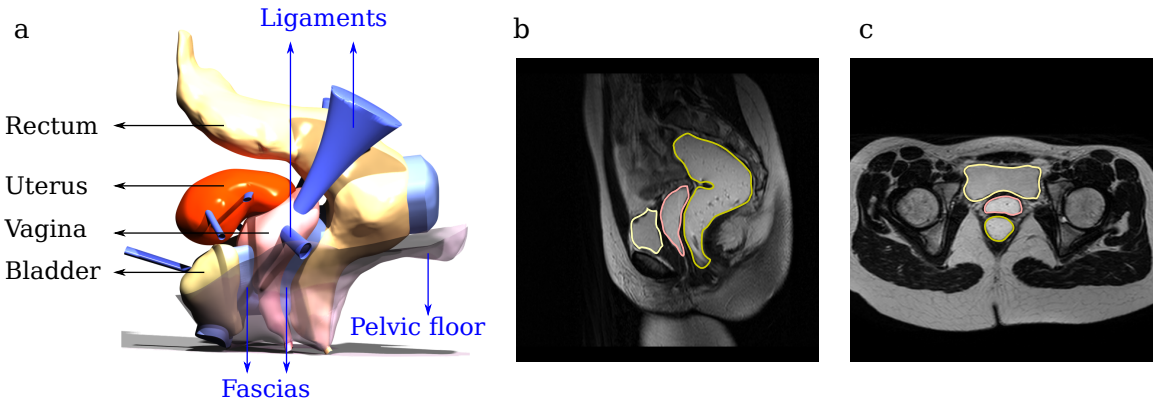

FIGURE 1 Pelvic system: (a) 3D rendered model (sagittal view) (b,c) T_2-weighted static MRI of a healthy witness (sagittal and transverse plane respectively, spatial resolution = 0.59 mm pixel $^{-1}$, slice thickness = 4 mm and 512×512 pixels). Structures in blue are involved in simulation, but are not observable in MRI.

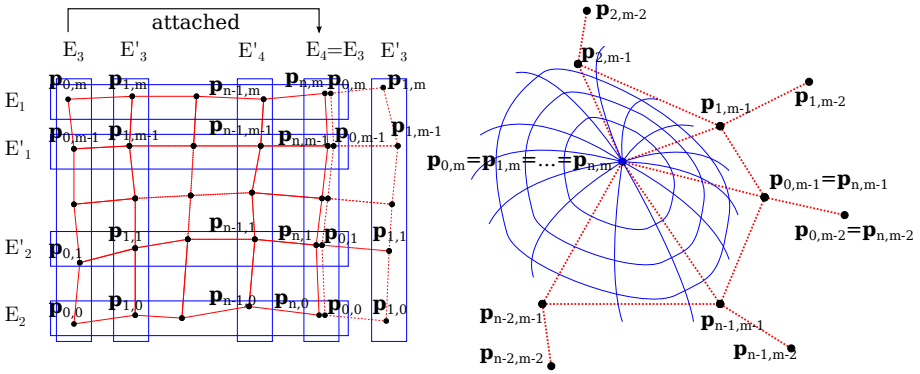

FIGURE 2 Arrangement of the control points for a closed surface: two sides are attached to form a tube-like shape (left) and two ends of the tube are joined to close (right). The red grid shows the control net. The blue frames indicate the rows and the columns (left). The blue curves illustrate isolines on surface in $u-$ and $v-$ direction (right).

- a global transformation $\mathbf{T} \in \mathbb{R}^{4\times4}$ applied to an initial surface: $\mathcal{S}^*(u,v) = \mathbf{T}\mathcal{S}^0(u,v)$, where $\mathcal{S}^0$ is the initial surface and $\mathcal{S}^*$ the deformed surface with respect to the parameters of $\mathbf{T}$ (12 maximum). Let $[p_x, p_y, p_z, 1]$ be the homogeneous coordinates of a point $\mathbf{p}^0$ on a surface, and $[T_x, T_y, T_z]$ a translation of rigid body, $\mathbf{T}$ is defined with homogeneous coordinates:

$$\mathbf{p}^* = \begin{bmatrix} R_{00} & R_{01} & R_{02} & T_x \\ R_{10} & R_{11} & R_{12} & T_y \\ R_{20} & R_{21} & R_{22} & T_z \\ 0 & 0 & 0 & 1 \end{bmatrix} (\mathbf{p}^0 - \mathbf{c}) + \mathbf{c}, \qquad (2)$$

  where a local origin $\mathbf{c}$ can be used to perform object-centred transformation;

- control points of the surface: $\mathcal{P}(\{\mathbf{p}_{i,j}\}) = \mathcal{S}^*$. Obviously, with this parametrization the surface has more variability and more DOFs.

In the literature, various types of parametrization have also been developed, such as Freeform Deformation (FFD) [29] and space deformation based on Radial Basis Functions (RBFs) [3, 2]. They have the potential for the deformation of complex geometries. In our application, using the first two types of parametrization, a multi-scale strategy (global and local) is implemented to improve the quality of registration.

2.2 | Cost function and Optimization

The extension of the method from 2D to 3D does not change the definition of virtual image and cost function. As given in [11, 10], a level set function $\mathcal{L} : d \in \mathbb{R} \rightarrow \mathbb{R}$ is defined by

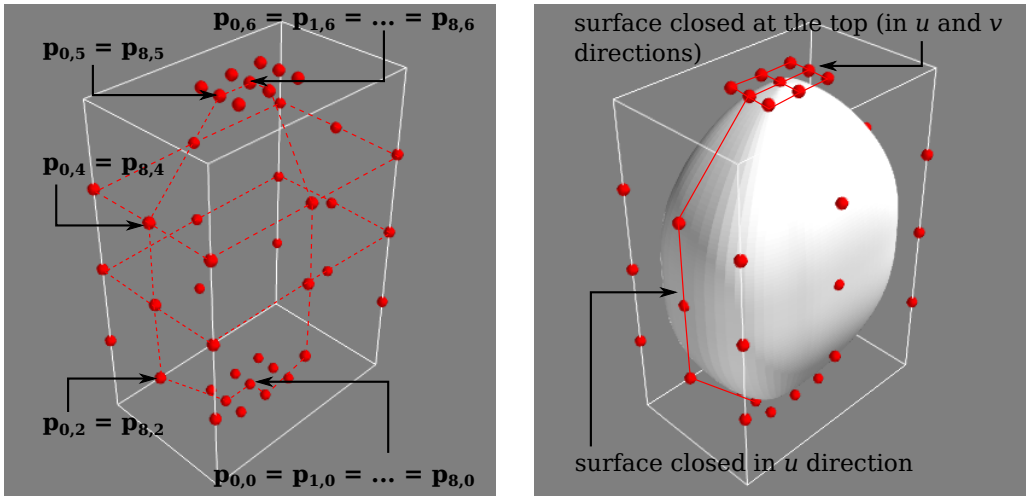

FIGURE 3 Prototypical model $\mathcal{M}_s$ of organ - control points in red.

the following equation:

$$\mathcal{L}(d) = \begin{cases} A_{max} & if \quad d < 0, \\ A_{min} + \frac{A_{max} - A_{min}}{2} \times (1 + cos(\frac{\pi d}{\tau})) & \\ & if \quad 0 \leq d \leq \tau, \\ A_{min} & if \quad d > \tau. \end{cases} \tag{3}$$

where d is the distance from a position $\mathbf{x}$ to the target surface. A_{max}, A_{min} represent the maximum and minimum of gray level, near the boundary of the surface. In our case, these are the grey levels inside and outside of the organs. The constant τ represents the width of the region, the gray level of which varies from A_{max} to A_{min}. In fact, the level set function is an intensity profile that simulates the variation of gray level in the neighbourhood of the boundary, Figure 4 gives an illustration.

To clarify the concept and computation of the cost function and its optimization, we illustrate firstly this technique with a 1D example. Figure 5 illustrates the real image intensity and an associated level set function, located near a point on the contour. This example will be used to show the optimization process in 1D manner.

The idea is to find the optimal shifting of the level set function (red one) so that it best fits the real image intensity (yellow one). The optimized shifting indicates where the contour is located. The optimum is obtained by minimizing the cost function that compares these two functions on a set of sampled points. Let $\{\mathbf{x}_i = \frac{\tau}{n-1} \times i | i = 0, ..., n-1\}$ be a uniform sampling of n points in the region of width τ, the following equation defines the cost function:

$$\begin{aligned} \mathcal{F}(d) &= \sum_{i=0}^{n-1} [I_R(\mathbf{x}_i + d) - I_V(\mathbf{x}_i)]^2 \\ &= \sum_{i=0}^{n-1} [I_R(\frac{\tau}{n-1} \times i + d) - \mathcal{L}(\frac{\tau}{n-1} \times i)]^2, \end{aligned} \tag{4}$$

where I_R is the interpolated intensity of the real image and I_V is the virtual one. As shown in Figure 6 , while the level set function was being shifted along the abscissa, the cost function can be computed for a given value d. By minimizing the cost function, the optimal position can be obtained. Compared to the choice of A_{max} and A_{min}, which is determined by each image data, the value of τ influences where the contour is located, empirically a value between 2 and 3 pixels is suitable for our data set.

In a similar way to 1D and 2D, to model the surfaces, the cost function is defined by the difference between the real and virtual images. It should be noted that the comparison is performed in the neighbourhood of the CAD surface, not in the whole domain of images. Concretely, let d be the distance from a neighbouring point to the surface $\mathcal{S}$, a set of discrete points can be sampled and their coordinates can be given by surface parameters (u, v) and the distance d:

$$\mathbf{x}(u, v, d) = \mathcal{S}(u, v) + d\mathbf{n}(u, v), \tag{5}$$

where $\mathbf{n}$ is a normal to the surface. The gray level of the virtual image at position $\mathbf{x}$ can be computed directly:

$$I_V(\mathbf{x}) = I_V(u, v, d) = \mathcal{L}(d). \tag{6}$$

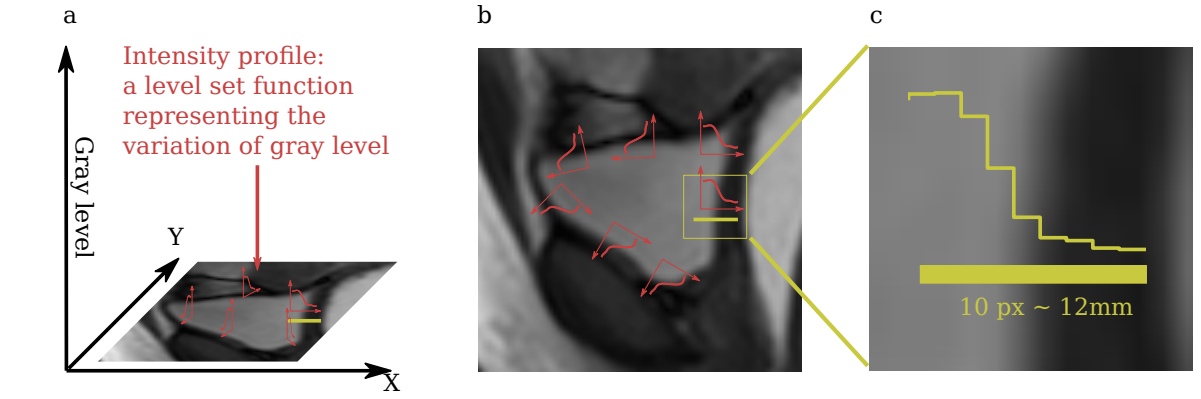

FIGURE 4 Illustration of the intensity profile (level set function). (a,b) The intensity profile is associated to the contour, simulating the variation of gray level, along the contour. (c) Gray level of the real image, from the inside to the outside (A_{max} to A_{min}).

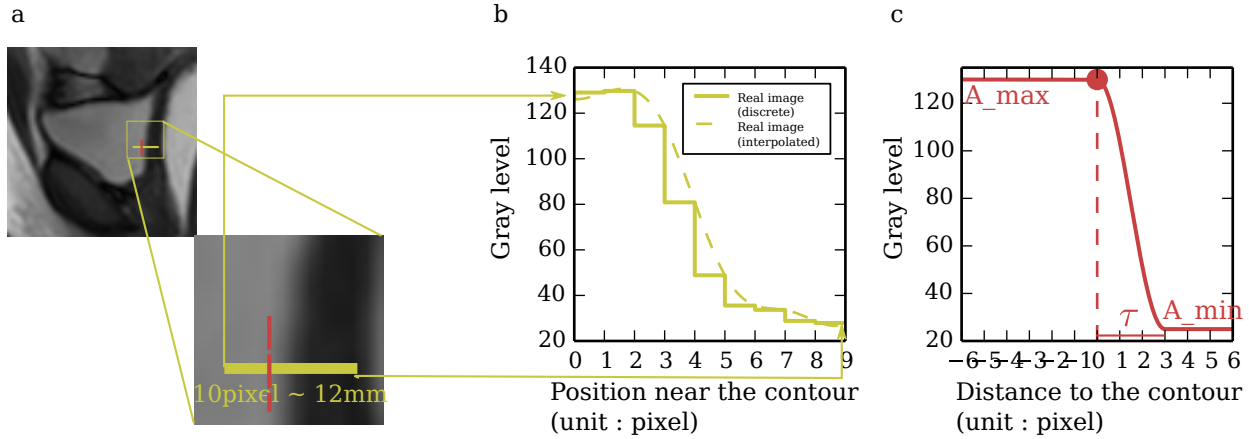

FIGURE 5 Definition of the intensity profile (level set function). 1D example: real image intensity (yellow) and level set function (red), defined in the neighbourhood of the contour.

Thus, the cost function is defined by the following equation:

$$E_{image} = \sum_u \sum_v \sum_d [I_R(\mathbf{x}(u,v,d)) - I_V(\mathbf{x}(u,v,d))]^2$$
$$= \sum_u \sum_v \sum_d [I_R(\mathbf{x}(u,v,d)) - \mathcal{L}(d)]^2, \quad (7)$$

where I_R corresponds to the interpolated gray level of the real image. As aforementioned, the optimization takes place at two scales: a global optimization aiming to find the right transformation matrix $\mathbf{T}$ and a local optimization varying control points $\{\mathbf{p}_{i,j}\}$. The implemented optimization is a gradient-based algorithm.

2.3 | Analysis using prototypical images

To analyse the performance of registration method and evaluate the uncertainty, a generic geometrical model was created and 3D prototypical images were generated from this geometry. With different initial values of parameters of the matrix $\mathbf{T}$, the method is able to find the best alignment between the geometry and image (according to the initial configuration).

To define the prototypical geometry, 9×4 control points are uniformly spaced on a grid, except several joining points. The computed generic shape is a bell-like open surface. Let us consider the bidirectional grid $\{\mathbf{p}_{i,j}\}$, for a fixed value $\bar{j}$, the control point in the first row $\mathbf{p}_{0,\bar{j}}$ is rotated about Z-axis (every 45°) to form a semi-closed surface (Figure 7). The mean times, for a fixed value $\bar{i}$, $\mathbf{p}_{\bar{i},j=0,1,2}$ are uniformly arranged following Z-axis. Besides $\mathbf{p}_{0,3}$ is repeated 9 times at the top, the grid has thus 9×4 control points.

The position of control points is given by the following formula with a rotation angle dependent on i, $\theta = i * \pi/4, i \in$

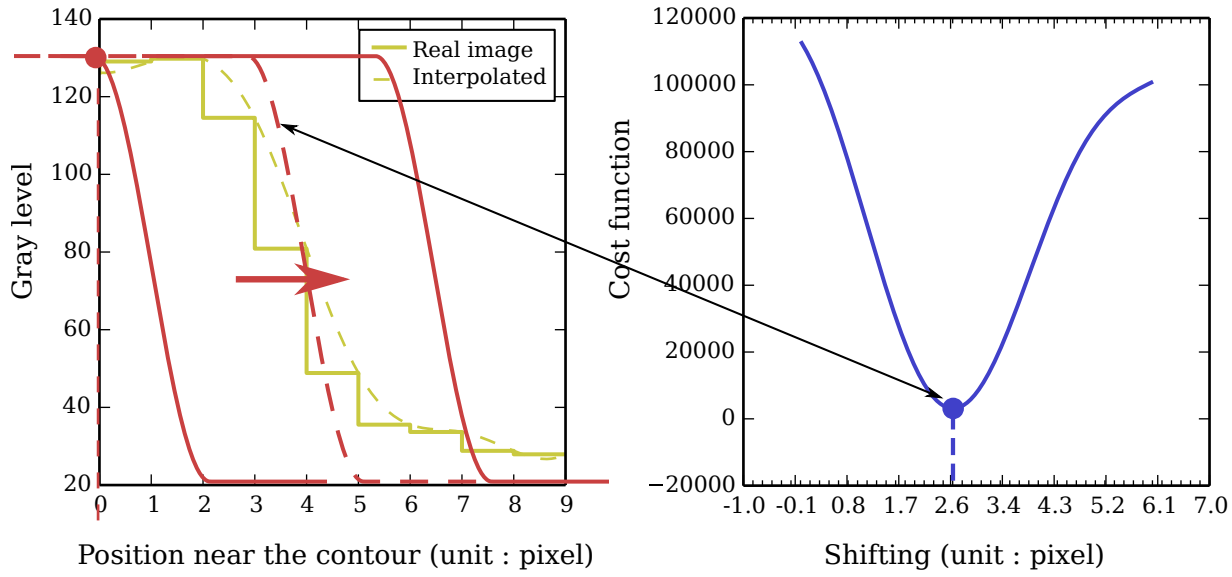

FIGURE 6 Illustration of the optimization in 1D manner : $A_{max} = 130.0$, $A_{min} = 25.0$ and $\tau = 3.0$. The cost function on the right reaches its minimum for a shifting d of 2.6 pixel, which corresponds to the dashed red curve on the left.

$[0, 8]$:

$$\mathbf{p}_{i,j} = [x(\theta), y(\theta), z(j)]. \tag{8}$$

The coordinates x and y have value -0.5, 0.0 or 0.5, with respect to the rotation angle θ. The z value depends on the index of column j. For the control points $\{\mathbf{p}_{i,j} | j < 3\}$,

$$x(\theta) = \begin{cases} -0.5 & if \quad \cos(\theta) < 0, \\ 0.0 & if \quad \cos(\theta) = 0, \\ 0.5 & if \quad \cos(\theta) > 0 \end{cases}$$

$$y(\theta) = \begin{cases} -0.5 & if \quad \sin(\theta) < 0, \\ 0.0 & if \quad \sin(\theta) = 0, \\ 0.5 & if \quad \sin(\theta) > 0 \end{cases}$$

$$z(j) = -0.5 + 0.5 * j. \tag{9}$$

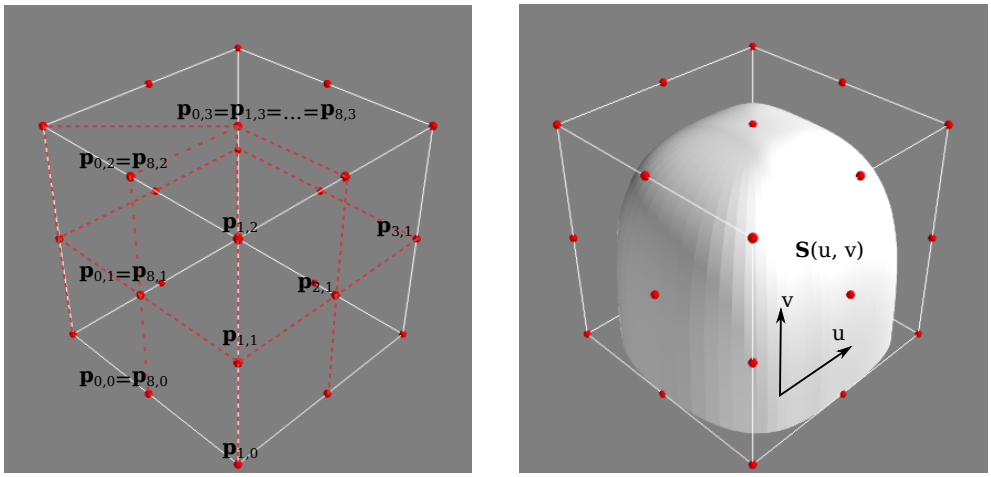

FIGURE 7 Definition of the prototypical geometry.

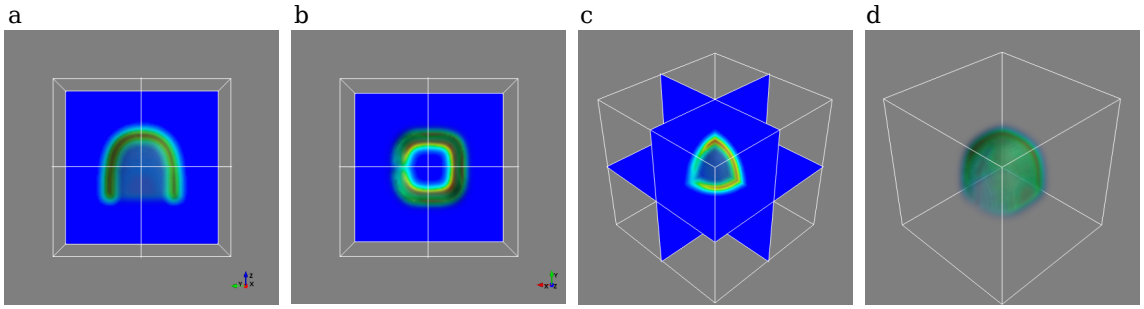

FIGURE 8 Generation of the 3D prototypical image of $100 \times 100 \times 100$ pixels and 1 mm pixel^{-1}: (a) X-axis view (b) Z-axis view (c) Perspective view (d) The image volume.

For the joining points on the top $\{\mathbf{p}_{i,3} | \forall i \in [0, 8]\}$: $\mathbf{p}_{i,3} = [0.0, 0.0, 0.5]$. Figure 7 shows the geometry definition.

The corresponding 3D image is then generated from the geometry. The image is defined in the vicinity of the surface with a thickness of 6 mm, its gray level varies from 1 to 0 (Figure 8). Thus, we can dismiss initially problems related to initialization, image artefact and the complexity of shapes. However, it is useful to validate the method in a controllable way: the inputs and theoretical values are known *a priori*.

Three test cases have been carried out: a scaling, a translation and an affine transformation, their parameters have been optimized respectively. The global transformation (4×4 matrix $\mathbf{T}$) is applied to all the control points of the surface. The origin $\mathbf{c} = [c_x, c_y, c_z, 1]$ is the center of the image, and the parameters R_{ij}, T_k are optimized using a gradient descent algorithm in each case.

2.3.1 | Scaling

The first test case relates to the diagonal values of a transform matrix. The following values were imposed to obtain the initial model: $R_{00} = 2.0, R_{11} = 2.0, R_{22} = 1.5$. Thus, beginning with the identity matrix, the theoretical values of R_{00}, R_{11} and R_{22} should correspond to the diagonal values of the inverse of imposed transformation once the optimization reaches its convergence:

$$\mathbf{T}_0 = \begin{bmatrix} R_{00} = 0.5 & 0 & 0 & 0 \\ 0 & R_{11} = 0.5 & 0 & 0 \\ 0 & 0 & R_{22} = 0.67 & 0 \\ 0 & 0 & 0 & 1 \end{bmatrix}. \tag{10}$$

As shown in Figure 9 and 10 , the obtained experimental values are $[0.52, 0.52, 0.70]$.

2.3.2 | Translation

The second test consists in applying only a rigid body translation to the prototypical model. The following values of $[T_x, T_y, T_z]$ were imposed to obtain the initial model: $[-10.0, -15.0, 10.0]$. At the end of the optimization, the theoretical values should be

$$\mathbf{T}_0 = \begin{bmatrix} 1 & 0 & 0 & T_x = 10.0 \\ 0 & 1 & 0 & T_y = 15.0 \\ 0 & 0 & 1 & T_z = -10.0 \\ 0 & 0 & 0 & 1 \end{bmatrix}. \tag{11}$$

As shown in Figure 11 and 12 , the experimental values are $[9.36, 15.01, -8.79]$. These results will be discussed later in this section.

2.3.3 | Scaling and rotation

The last test is to apply a scaling combined with a rotation to the prototypical model. 9 parameters of the transformation matrix are taken into account. We omit the translation in the following for two reasons:

- In our application, the initial model is positioned at the center of mass of the target volume (detailed in Section 3.1.1). The extra three degrees of freedom are not needed;
- A parameter normalization is essential for including translation, which is not evident, especially when the initial model is not close to the prototypical image. And this is not the concern of our method.

To define the initial model, the prototypical one is first rotated around the X-axis by 20°, and then scaled in the three directions.

The following values are applied to the prototypical model: $R_{00} = 1.5$, $R_{11} = 1.5\cos(20°)$, $R_{12} = -1.2 * \sin(20°)$, $R_{21} = 1.5\sin(20°)$, $R_{22} = 1.2\cos(20°)$. The theoretical values at the

Errors				Scaling				Translation				Scaling+Rotation				Resolution			
R_{00}	R_{01}	R_{02}	T_x	0.02	-	-	-	-	-	-	0.64 mm	0.01	0.01	0.04	-	0.01	0.01	0.04	-
R_{10}	R_{11}	R_{12}	T_y	-	0.02	-	-	-	-	-	0.01 mm	0.00	0.03	0.01	-	0.00	0.03	0.01	-
R_{20}	R_{21}	R_{22}	T_z	-	-	0.03	-	-	-	-	1.21 mm	0.05	0.02	0.04	-	0.05	0.02	0.05	-

TABLE 1 Table of absolute errors of the presented three tests.

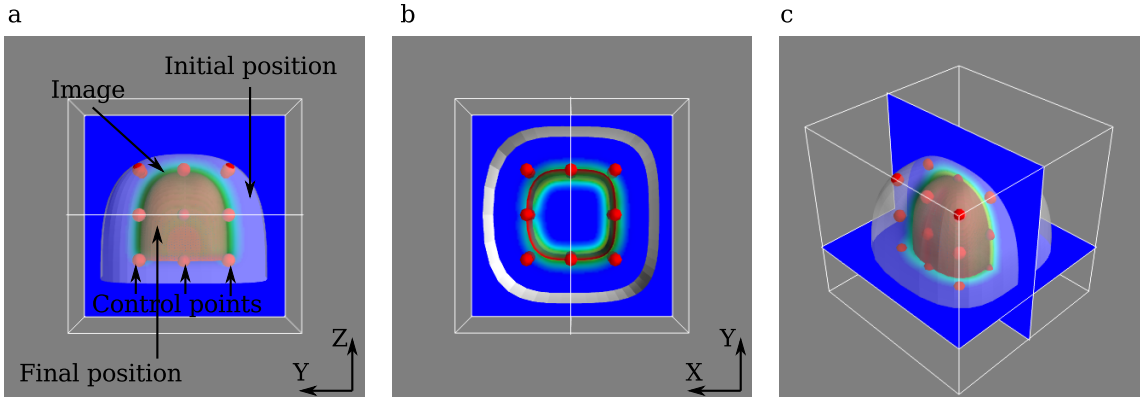

FIGURE 9 Visual illustration of the scaling optimization:(a) X-axis view (b) Z-axis view (c) Perspective view.

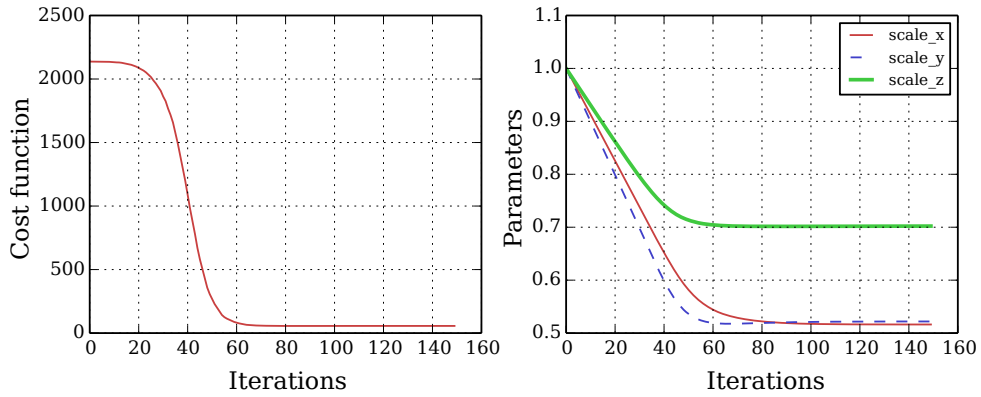

FIGURE 10 Illustration of the convergence of the scaling optimization: cost function and parameter values with respect to the iteration (initial value = 2137.2 and final one = 56.3).

end of optimization should be

$$\mathbf{T}_0 = \begin{bmatrix} 0.67 & 0 & 0 & 0 \\ 0 & 0.63 & 0.23 & 0 \\ 0 & -0.28 & 0.78 & 0 \\ 0 & 0 & 0 & 1 \end{bmatrix}. \quad (12)$$

The obtained experimental values are

$$\begin{bmatrix} 0.68 & -0.01 & 0.04 & 0 \\ 0 & 0.66 & 0.24 & 0 \\ -0.05 & -0.30 & 0.82 & 0 \\ 0 & 0 & 0 & 1 \end{bmatrix}$$

(see Figure 13 and 14 for the illustrations).

Table 1 shows the absolute errors between theoretical and experimental results. Being used in these tests, the prototypical image is generated from the prototypical model in a discrete way : discrete points are sampled in the vicinity of the surface to identify the virtual image intensity. However, a Gaussian filter is applied to smooth out the 3D image and to fill in missing voxels, therefore it is not exactly the same as the virtual image defined by level set function $\mathcal{L}$ (which is usually the case in real applications). This explains the slight difference between

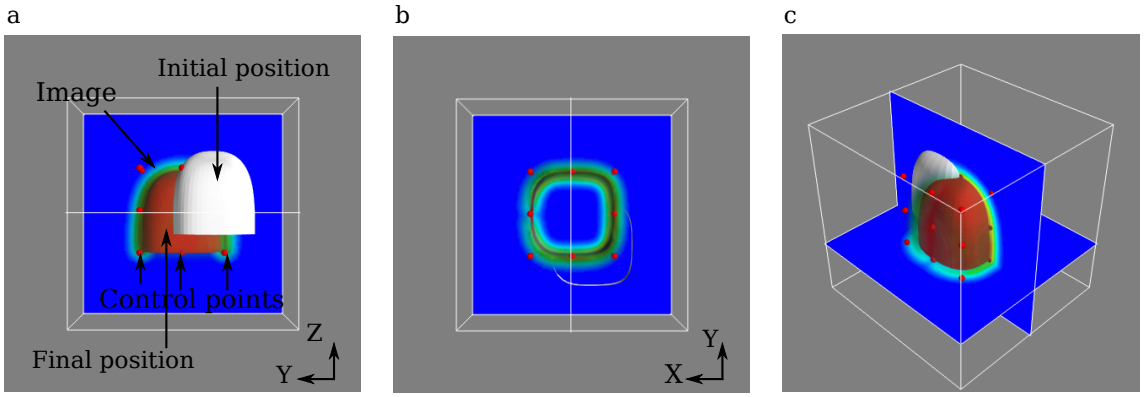

FIGURE 11 Visual illustration of the translation optimization:(a) X-axis view (b) Z-axis view (c) Perspective view.

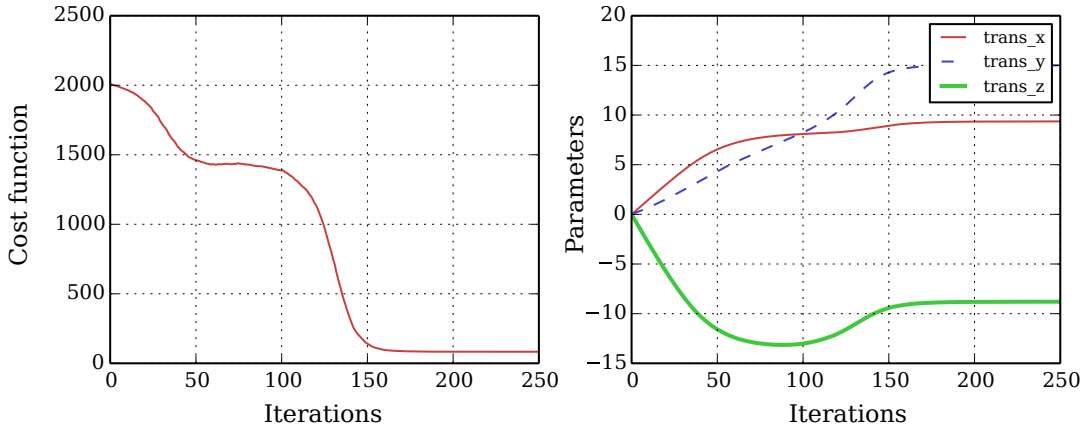

FIGURE 12 Illustration of the convergence of the translation optimization: cost function and parameter values with respect to the iteration (initial value = 2008.8 and final one = 83.3).

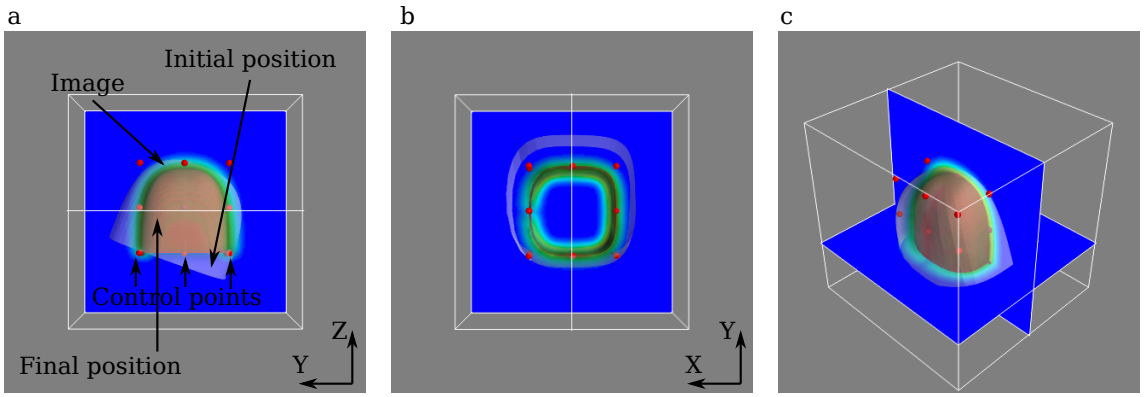

FIGURE 13 Visual illustration of the rotation optimization:(a) X-axis view (b) Z-axis view (c) Perspective view.

theoretical and experimental values. The amplitude and thickness of a defined level set have also some influence on optimal values. Moreover, in the case of translation, the initial model is quite far from the final position. On the other hand, thanks to our method, we can show the influence of image resolution is

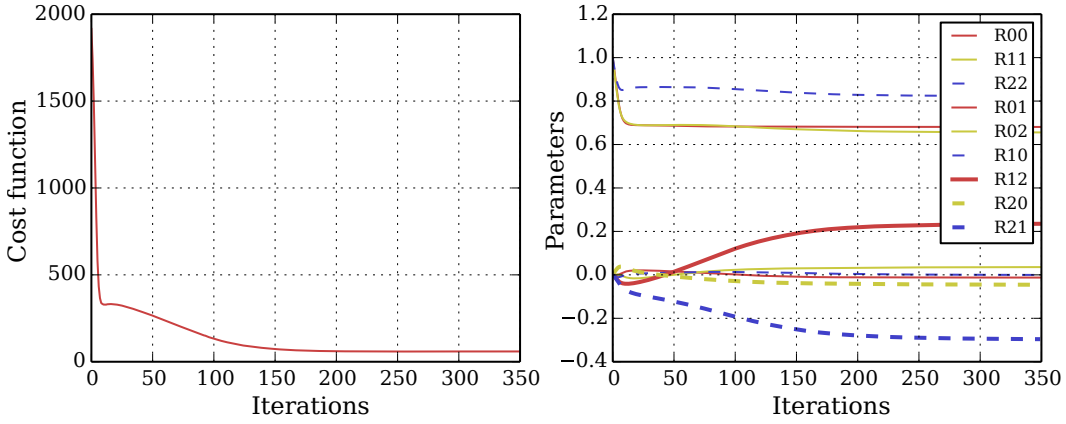

FIGURE 14 Illustration of the convergence of the rotation optimization: cost function and parameter values with respect to the iteration (initial value = 1915.4 and final one = 59.2).

not preponderant. In this example, the image resolution is multiplied by 2, and the same optimization is performed with the finer image ($200 \times 200 \times 200$ pixels, 0.5 mm pixel^{-1}). Finally, the experimental values have slightly changed in the order of 10^{-3} (last column of Table 1). In fact, the optimization is based on virtual image, which is linked with the geometry. It can have a higher resolution than the real image and the gray level in the real image is interpolatory. Thus, the algorithm has a sub-voxel precision.

3 | RESULTS AND DISCUSSIONS

3.1 | Application to the geometric modelling of the vagina

In this section, we will apply the previous validation tests to clinical data (MRI) to reconstruct a 3D model of pelvic organs. Generally, the robustness of detection algorithms depends strongly on the initialization and the quality of images. Thus, pre-processing and initialization are necessary. Concerning the pre-processing, thresholding and mathematical morphology operators are applied to extract the organ volumes from the raw images. With regard to initialization, it is important to better position the generic model $\mathcal{M}_s$ to obtain the initial model $\mathcal{M}_i$. For these purposes, $\mathcal{M}_s$ is first oriented along the principal axes of the volume containing the target organ. Then, a global transformation is applied and optimized to align as best as possible the model with the volume to obtain a well-defined $\mathcal{M}_i$.

3.1.1 | Image pre-processing

This part introduces briefly the thresholding and morphological operation [32] applied to the raw image data. Practically, the choice of threshold is manually defined for each organ (by click in the median plane of MRI). Then an erosion results in a better isolated target, in every slice. Once a separated volume is obtained, a dilatation is used again to minimize the deviation from the raw image data. Lastly, the principal orientation of the organ can be computed using 3D image moments of different orders.

3.1.2 | Global scaling for initialization

As mentioned in Section 2.3, the geometry of organs is defined by closed B-Spline surfaces, similar to the prototypical model. Only the arrangement of control points is modified so that the surface is closed. Figure 3 illustrates a 9×7 control points net to define the generic model $\mathcal{M}_s$.

The global scaling permits to get a better initialization ($\mathcal{M}_i$) before locally adjusting control points. Once the orientation of the model has been performed, a change of scales is applied to align the model and the separated volume as close as possible. This scaling is optimized by varying the diagonal values of the transformation matrix. The gradient descent algorithm is stopped once the variation of the parameters becomes stable (less than 0.01). The choice of threshold (0.01) is not of critical importance because the shape of $\mathcal{M}_s$ is generic, which cannot be aligned perfectly with the volume. Thus, a fast approximate global scaling is sufficient to obtain a desired initial model $\mathcal{M}_i$.

3.1.3 | Local registration

The local registration consists in deforming the initial model $\mathcal{M}_i$ locally by modifying the positions of its control points. This step continues to minimize the cost function (Equation 1 and 7), which makes it capable of obtaining a finer geometrical reconstruction of organs.

During the optimization, control points move independently and in 3-Dimension. Meanwhile, some constraints are imposed to ensure geometric continuity. In Figure 3 , control points joined together at the lateral side, are removed from the degrees of freedom. They are recomputed as the middle of the adjacent two points: $\mathbf{p}_{0,\bar{j}} = \mathbf{p}_{8,\bar{j}} = (\mathbf{p}_{1,\bar{j}} + \mathbf{p}_{7,\bar{j}})/2$. At the top, because $\mathbf{p}_{0,6}$ and $\mathbf{p}_{0,0}$ are repeated 9 times, and their neighbouring points $\{\mathbf{p}_{i,5}\}$ should be coplanar. The average displacement of these points is imposed.

Figure 15 and 16 illustrate the global initialization and local registration performed on the volume of the vagina (512× 512 pixels, 0.59 mm pixel^{-1} and 4 mm between slices). With a close initialization, the Model-to-Image Registration can be convergent to the separated volume. The choice of gradient descent factors is usually highly problematic, especially with the anisotropic voxels, the cost function is relatively not a smooth and convex one. A gradient descent algorithm is used to execute the optimization. We decided to use the maximal displacement of all the control points (DOFs) as a stop criterion for the optimization.

3.2 | Reconstruction of pelvic system of multiple patients

In this part, the same registration algorithm is applied to reconstruct three principal organs (bladder, vagina and rectum) from the MRI of four patients. We would like to demonstrate the following points through these datasets:

- stability and reproducibility of the algorithm
- direct usage of the model with meshing tool
- evaluation of uncertainties.

With the empirical thresholds, the algorithm succeeds in finding the final models corresponding to the volumes. The most important one is that they are consistent, smooth and compatible to be imported into other tools for meshing and simulation. Figure 17 shows the reconstructed models of 4 witnesses, which are converted directly into regular mesh (NETGEN [27]). We can observe that pelvic organs have large inter-variability; however, the quality of geometry is ensured. Then, we are interested in the accuracy of the geometry by evaluating its deviation from the MRI.

This results in a quantitative comparison: the reconstructed model is confronted with the geometry in the form of a point cloud obtained by manual MRI segmentation, performed by doctors. Manual segmentation is performed with the AVIZO software. Then, the models were imported into the CAD software CATIA (https://www.3ds.com/fr/produits-et-services/catia/), which allows us to perform an accurate analysis of the deviation.

The analysis involves the measurement of point-to-point distances. All the points on the manually segmented surface are projected to the reconstructed model. Each organ is evaluated on approximately 10, 000 points (Figure 18). We show the average and standard deviations of each organ and patient in Table 2 .

In these examples, as can be seen, the ends of the vagina and rectum are difficult to identify by the proposed algorithm. There are such fine and sometimes blurred areas that only the doctor manages to identify them manually. Other difficulties are encountered, caused by the presence of wrinkles and spots in the rectum [11]. The model of the rectum is thus restricted to correspond to the lower part in contact with the vagina. However, this missing upper part does not lead to deficiency in the numerical simulation. We would like to mention other limitations of the registration method in the next section.

3.3 | Discussions

It should be emphasized that in an FE simulation, the point cloud or raw mesh is not usable. An operator must manually perform time-consuming surface creation and repairing to obtain a functional geometry which would not correspond to the original image data. At this stage, we are able to have a relatively simple, image-guided smooth geometric model that is usable for remeshing and prospective FE analysis. As mentioned in Section 1, the standard technique Marching Cubes [19] cannot be suitable for the FE analysis in a straight way. Despite the fact that the extended Marching Cubes [15] has succeeded in eliminating the terracing artefact and generating feature-sensitive triangle meshes, the triangle complexity depends on the volume resolution. More importantly, it is difficult to perform adaptive remeshing with the surface mesh. A parametric CAD model will be a better support for creating tetrahedron meshes for FE simulation.

The pelvic system is complex, which implies the main issue of the presented B-Spline model: it does not meet the need for defining highly complex boundary conditions, in order to perform a meaningful simulation. These boundaries consist of many different parts: the zones subject to displacements, or a distribution of pressure; the zones where a structure can contact another one. These contacts involve some missing suspension devices hardly visible in MRI : ligaments and fasciae (the blue parts in Figure 19).

To deal with this issue, a more complex generic geometrical model is required. For example, we used 3D geometry created manually in CATIA for the numerical simulation, which contains multi-patch structures (Figure 19). On this model, the attachment of fasciae and ligaments is well defined thanks to specific patches.

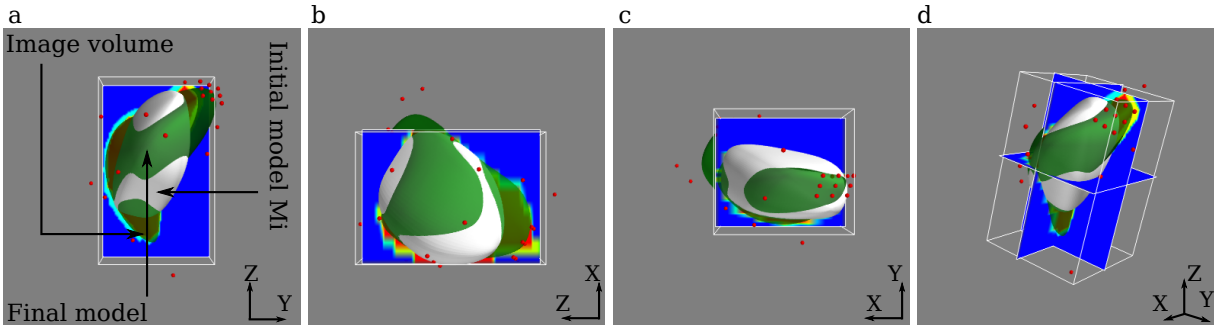

FIGURE 15 Visual illustration of the local registration on the volume of vagina : initial model in white and final model in green. (a) X-axis view (b) Y-axis view (c) Z-axis view (d) Perspective view.

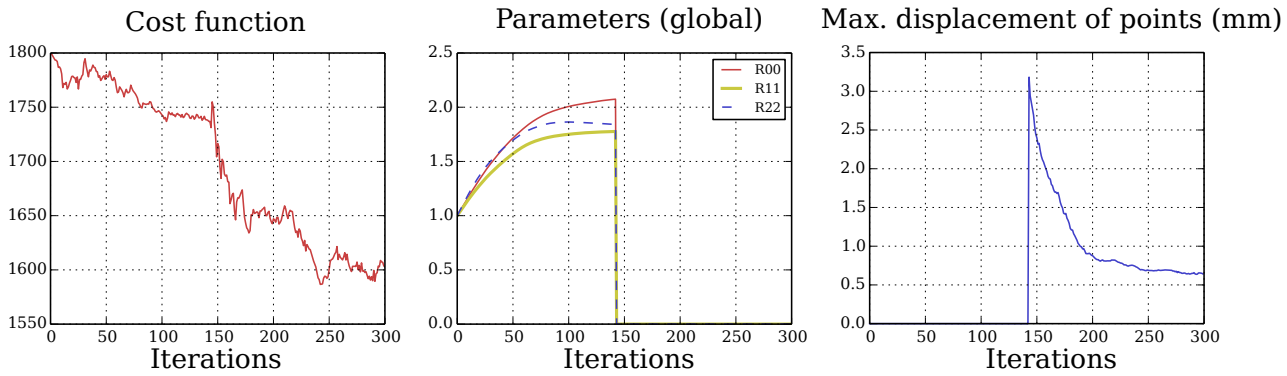

FIGURE 16 Illustration of the convergence of the global and local registration : (a) Cost function (b) Optimized parameters during global scaling (c) Maximum displacement of control points in mm. The first 140 iterations correspond to the global scaling.

	Organ	Average deviation (mm)	Standard deviation (mm)
Witness 1	Bladder	2.67	1.76
	Vagina	1.62	1.35
	Rectum	3.33	2.56
Witness 2	Bladder	2.43	2.27
	Vagina	1.64	1.38
	Rectum	2.73	2.30
Witness 3	Bladder	1.59	1.28
	Vagina	1.23	1.04
	Rectum	2.73	2.12
Witness 4	Bladder	2.76	2.27
	Vagina	2.73	2.39
	Rectum	2.79	2.71

TABLE 2 Table of deviation measurements based on point-wise distances. The resolution of used MRI is 0.59 mm pixel^{-1} or 0.73 mm pixel^{-1}, and the thickness between slices is from 3 to 4 mm.

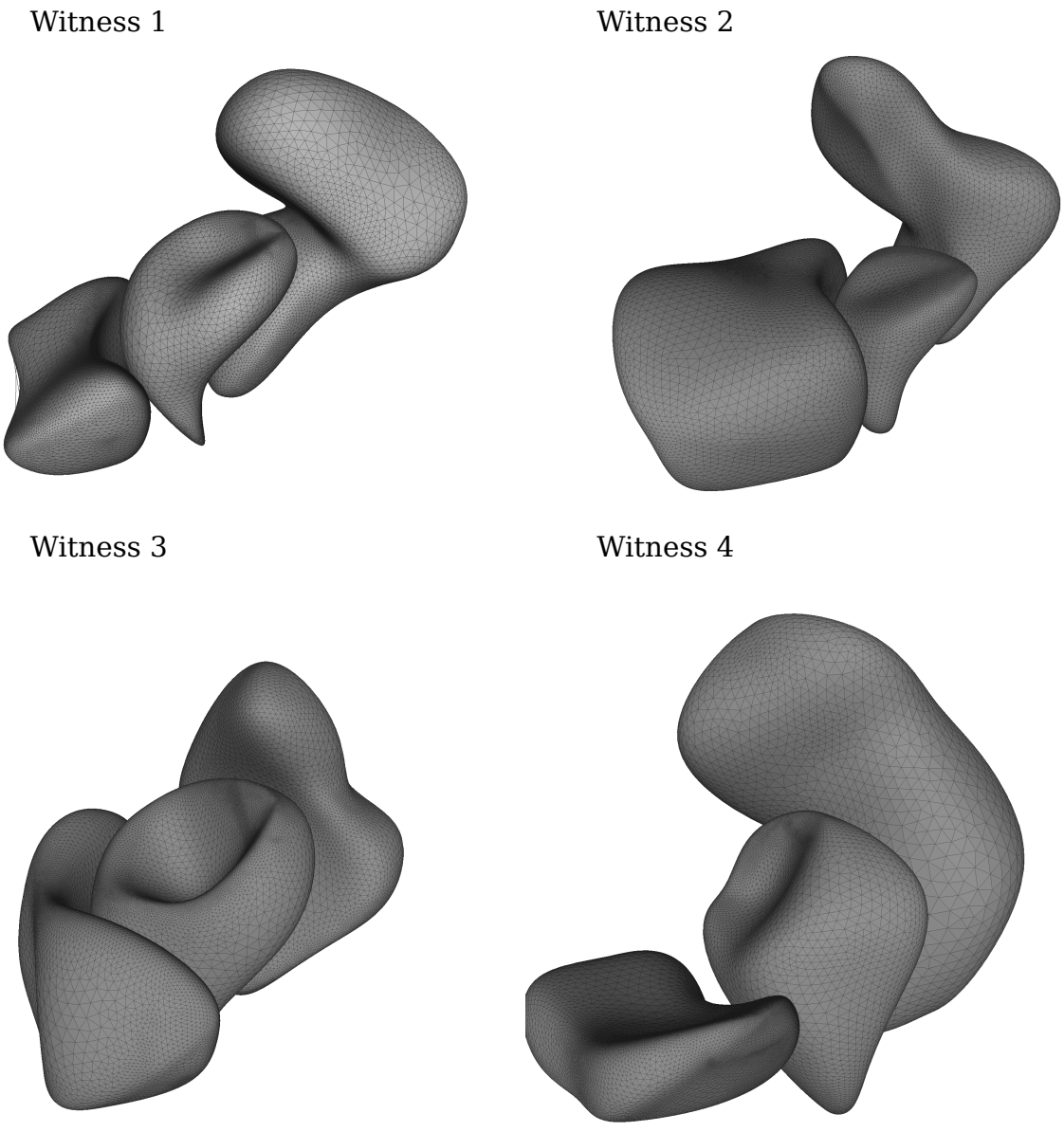

FIGURE 17 Reconstruction of pelvic organs (bladder, vagina, rectum).The final geometrical model is exported to STEP file and then processed by meshing tool NETGEN [27]. The concave shape at the top of the vagina is due to the absence of the uterus.

The first intuition is to use all the control points as DOFs for the registration. However, contrary to the simplified model, this model has a large number of control points. Table 3 shows the complexity of this model. Hence, it is more reasonable to find a DOF reduction and refinement technique.

In 2D version [11], control points were adaptively added and removed during the optimization of B-Spline contours.It was possible to detect fine details of geometry, by avoiding meanwhile unnecessary control points. Unfortunately, this technique cannot be applied to the current 3D model, due to the properties of B-Spline surface. Indeed, an insertion or

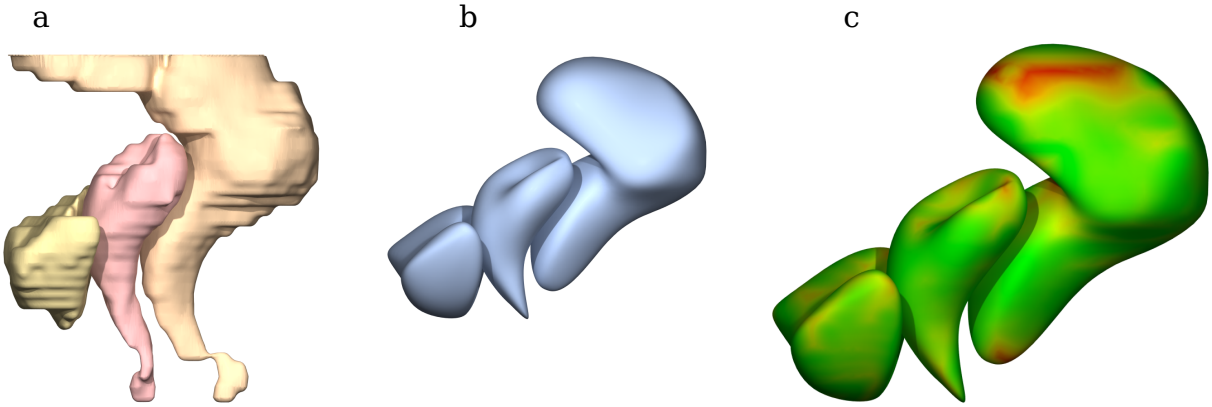

FIGURE 18 Comparison between two models (deviation measured by point-wise distances): (a) manually segmented model (b) reconstructed model by registration method (c) cartography shows the distances point-to-point in mm between (a) and (b) (red color represents high deviation and the average value for the three organs is 2.48 mm).

removal of control points will affect the entire line (or column) of the control net grid. We cannot arrange a single control point locally in an exact position because their form should remain bidirectional. This forced us to find a fixed number of control points, which is a trade-off between accuracy in terms of "geometry" and functionality of the model (compatible to simulation). An alternative approach has been proposed, which enables the local refinement of the control grid [1]. In [14], an adaptive refinement technique was performed in a hierarchical manner to describe geometries and displacements.

Another approach to enrich a simplified model to achieve the model shown in Figure 19 , is to use the T-spline surfaces. This concept was introduced by [30, 28] and overcomes the limitations of B-Spline or NURBS model. The control grid is less well structured and more flexible: the number of points in rows (or columns) may be different. In fact, a row and a column may have an intersection of "T" form. Hence, local refinement would be possible with this modelling. However, it is not evident to implement a T-spline model. Moreover, the boundaries should be defined more clearly using meaningful patches.

The third approach consists in using some space deformation techniques, such as Radial Basis Functions (RBF) [3, 2]. The idea is to deform all the structures well-defined simultaneously and the deformation is deduced from a few DOFs. Moreover, the DOFs themselves can be added during the registration. Combining RBF-based deformation and VIC method may bring promising results for complex geometry reconstruction from images. Let us reconsider the missing suspension structures mentioned at the beginning of this section. In the medical reality, there exists no way to identify these suspension devices by imaging techniques. Even in books of anatomy there are few common agreements on the position of these structures. Thus, anatomically it is impossible to define these positions precisely and adapted to each patient. However, we created a mechanically consistent model including these structures, after taking into account the description in an anatomy book (Figure 19). To ensure the plausibility of the boundary conditions with maximum precaution, the invisible structures would follow the space deformation, so that they would still be suitable for numerical simulation and adapted for a set of patients.

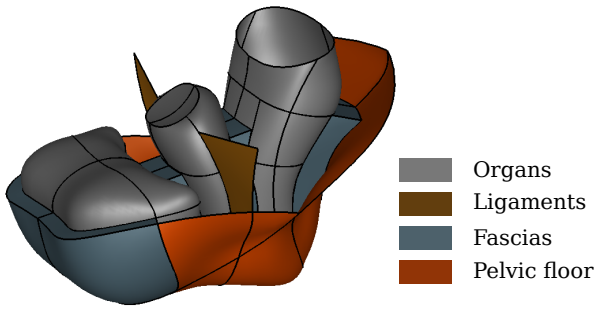

FIGURE 19 The complex generic 3D model.

Organ	Bladder	Vagina	Rectum
No. of patches	14	14	20
No. of control points	4608	1017	1098

TABLE 3 Statistics of geometry entities of the complex generic model.

4 | CONCLUSION AND PERSPECTIVES

In the presented paper, we present an approach to reconstruct the 3D geometrical model of pelvic organs from MRI. The main contribution is to obtain smooth, consistent and simulable 3D models by deforming an existed generic model, so it corresponds to the image data. The presented method allows us to obtain good results with a simplified 3D model (a single-patch B-Spline surface). A two-step strategy (global and local) has been developed for the optimization. Moreover, a major effort has been made to validate or compare these results with either prototypical cases or manual segmentation results.

By combining CAD modelling with VIC, the presented work is an important step forward for the VIC and for the Model-to-Image Registration. Thanks to the combination, the geometry modelling problem could be solved with flexible geometry parametrization and in a similar way to the Image Registration framework.

However, as discussed above, the principal challenge is now to introduce more complex geometry, and thus define where the organs, ligaments, fasciae should be connected and where the loadings should be applied. For this purpose, a geometrical morphing of all the structures based on RBF could be a promising approach.

Regarding the technical aspect, we would like to finalize the development to provide a user-friendly application, which can be easy-to-use in the clinical routine. Then, it would be possible to apply the method on more patient data to ensure the stability and robustness of the algorithm. The purpose of these enhancements is to reduce the gap between medical images and numerical simulation in real patient-specific cases.

References

[1] Bornemann, P. B. and F. Cirak, 2013: A subdivision-based implementation of the hierarchical b-spline finite element method. *Computer Methods in Applied Mechanics and Engineering*, **253**, 584–598.

[2] Botsch, M., L. Kobbelt, M. Pauly, P. Alliez, and B. Levy, 2010: *Polygon Mesh Processing.*. CRC Press Taylor & Francis Group.

[3] Buhmann, M. D., 2003: *Radial Basis Functions: Theory and Implementations.*. Cambridge University Press.

[4] Bump, R. C., A. Mattiasson, K. Bø, L. P. Brubaker, J. O. DeLancey, P. Klarskov, B. L. Shull, and A. R. Smith, 1996: The standardization of terminology of female pelvic organ prolapse and pelvic floor dysfunction. *American Journal of Obstetrics and Gynecology*, **175**, no. 1, 10–17.

[5] Cootes, T. F., C. J. Taylor, D. H. Cooper, and J. Graham, 1995: Active shape models - their training and application. *Computer Vision and Image Understanding.*, **61**, no. 1, 38–59.

[6] Cottrell, J. A., T. J. R. Hughes, and Y. Bazilevs, 2009: *Isogeometric analysis: toward integration of CAD and FEA*. John Wiley & Sons.

[7] Dell'oro, M., P. Collinet, G. Robin, and C. Rubod, 2013: Multidisciplinary approach for deep endometriosis: interests and organization. *Gynecol. Obstet. Fertil.*, **41**, no. 1, 58–64.

[8] Hamm, B. and R. Forstner, Eds., 2007: *Diagnostic Imaging - MRI and CT of the Female Pelvis*. Diagnostic Imaging, Springer-Verlag Berlin Heidelberg.

[9] Heimann, T. and H.-P. Meinzer, 2009: Statistical shape models for 3d medical image segmentation: A review. *Medical Image Analysis*, **13**, no. 4, 543 – 563.

[10] Jiang, Z., J.-F. Witz, P. Lecomte-Grosbras, J. Dequidt, S. Cotin, C. Rubod, C. Duriez, and M. Brieu, 2017: Multiorgan motion tracking in dynamic magnetic resonance imaging for evaluation of pelvic system mobility and shear strain. *Strain*, **53**, no. 2, e12224.

[11] Jiang, Z., J.-F. Witz, P. Lecomte-Grosbras, J. Dequidt, C. Duriez, M. Cosson, S. Cotin, and M. Brieu, 2015: B-spline based multi-organ detection in magnetic resonance imaging. *Strain*, **51**, no. 3, 235–247.

[12] Kass, M., A. Witkin, and D. Terzopoulos, 1988: Snakes: Active contour models. *International Journal of Computer Vision*, **1**, no. 4, 321–331.

[13] Kikinis, R., S. D. Pieper, and K. G. Vosburgh, 2014: *3D Slicer: A Platform for Subject-Specific Image Analysis, Visualization, and Clinical Support*, Springer New York, New York, NY. 277–289.

[14] Kleinendorst, S. M., J. P. M. Hoefnagels, R. C. Fleerakkers, M. P. F. H. L. van Maris, E. Cattarinuzzi, C. V. Verhoosel, and M. G. D. Geers, 2016: Adaptive isogeometric digital height correlation: Application to stretchable electronics. *Strain*, **52**, no. 4, 336–354.

[15] Kobbelt, L. P., M. Botsch, U. Schwanecke, and H.-P. Seidel, 2001: Feature sensitive surface extraction from volume data. *Proceedings of the 28th Annual Conference on Computer Graphics and Interactive Techniques*, ACM, New York, NY, USA, SIGGRAPH '01, 57–66.

[16] Lamecker, H. and S. Zachow, 2016: *Statistical Shape Modeling of Musculoskeletal Structures and Its Applications*, Springer International Publishing, Cham. 1–23.

[17] Lecomte-Grosbras, P., M. Nassirou-Diallo, J.-F. Witz, D. Marchal, J. Dequidt, S. Cotin, M. Cosson, C. Duriez, and M. Brieu, 2013: Towards a better understanding of pelvic system disorders using numerical simulation. *MICCAI, Nagoya, Japan*.

[18] Lee, C., S. Huh, T. A. Ketter, and M. Unser, 1998: Unsupervised connectivity-based thresholding segmentation of midsagittal brain mr images. *Comput Biol Med.*, **28**, no. 3, 309–338.

[19] Lorensen, W. E. and H. E. Cline, 1987: Marching cubes: A high resolution 3d surface construction algorithm. *Proceedings of the 14th Annual Conference on Computer Graphics and Interactive Techniques*, ACM, SIGGRAPH '87, 163–169.

[20] Luo, S., R. Li, and S. Ourselin, 2003: A new deformable model using dynamic gradient vector flow and adaptive balloon forces. *APRS Workshop on Digital Image Computing.*, 9–14.

[21] Mayeur, O., E. Jeanditgautier, J.-F. Witz, P. Lecomte-Grosbras, M. Cosson, C. Rubod, and M. Brieu, 2017: *Evaluation of Strains on Levator Ani Muscle: Damage Induced During Delivery for a Prediction of Patient Risks*, Springer International Publishing, Cham. 135–146.

[22] Mayeur, O., G. Lamblin, P. Lecomte-Grosbras, M. Brieu, C. Rubod, and M. Cosson, 2014: Fe simulation for the understanding of the median cystocele prolapse occurrence. *Biomedical Simulation*, volume 8789, 220–227.

[23] Paragios, N., Y. Chen, and O. Faugeras, Eds., 2006: *Handbook of Mathematical Models in Computer Vision*. Springer, Boston, MA, Boston, MA.

[24] Piegl, L. and W. Tiller, 1997: *The NURBS Book (2nd Edition)*. Monographs in visual communication, Springer-Verlag Berlin Heidelberg.

[25] Réthoré, J. and M. L. M. François, 2014: Curve and boundaries measurement using b-splines and virtual images. *Optics and Lasers in Engineering*, **52**, 145–155.

[26] Ruess, M., Z. Yosibash, N. Trabelsi, and E. Rank, 2011: Application of the finite cell method to patient-specific femur simulations. *PAMM*, **11**, no. 1, 117–118.

[27] Schöberl, J., 1997: Netgen - an advancing front 2d/3d-mesh generator based on abstract rules. *Computing and Visualization in Science.*, **1**, no. 1, 41–52.

[28] Sederberg, T. W., D. L. Cardon, G. T. Finnigan, N. S. North, J. Zheng, and T. Lyche, 2004: T-spline simplification and local refinement. *ACM SIGGRAPH 2004 Papers*, New York, NY, USA, SIGGRAPH '04, 276–283.

[29] Sederberg, T. W. and S. R. Parry, 1986: Free-form deformation of solid geometric models. *SIGGRAPH Comput. Graph.*, **20**, no. 4, 151–160.

[30] Sederberg, T. W., J. Zheng, A. Bakenov, and A. Nasri, 2003: T-splines and t-nurccs. *ACM SIGGRAPH 2003 Papers*, New York, NY, USA, SIGGRAPH '03, 477–484.

[31] Semin, B., H. Auradou, and M. L. M. François, 2011: Accurate measurement of curvilinear shapes by virtual image correlation. *European Physical Journal: Applied Physics*, **56**, no. 1, 10701–p1–10.

[32] Serra, J., 1988: *Image Analysis and Mathematical Morphology, Volume 2: Theoretical Advances.*. Academic Press.

[33] Shekhar, R., E. Fayyad, R. Yagel, and J. F. Cornhill, 1996: Octree-based decimation of marching cubes surfaces. *Visualization '96. Proceedings.*, 335–342.

[34] Xu, C. and J. L. Prince, 1998: Snakes, shapes, and gradient vector flow. *IEEE Transactions on Image Processing.*, **7**, no. 3, 359–369.

[35] Zhang, Y., Y. Bazilevs, S. Goswami, C. L. Bajaj, and T. J. Hughes, 2007: Patient-specific vascular nurbs modeling for isogeometric analysis of blood flow. *Computer Methods in Applied Mechanics and Engineering*, **196**, no. 29, 2943–2959.

□